Journal of Physics B: Atomic, Molecular and Optical Physics

PAPER

Cross sections for electron scattering from atomic lead

To cite this article: Matthew P van Eck *et al* 2020 *J. Phys. B: At. Mol. Opt. Phys.* **53** 015204

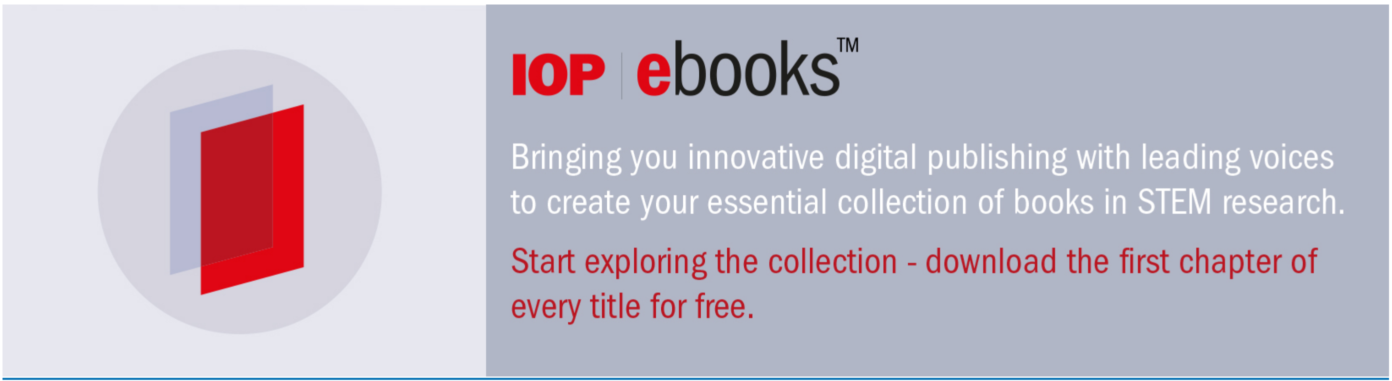

IOP Publishing

Journal of Physics B: Atomic, Molecular and Optical Physics

J. Phys. B: At. Mol. Opt. Phys. **53** (2020) 015204 (13pp)

https://doi.org/10.1088/1361-6455/ab53bc

Cross sections for electron scattering from atomic lead

Matthew P van Eck[1], Dmitry V Fursa[1], Igor Bray[1], Oleg Zatsarinny[2] and Klaus Bartschat[2]

[1] Department of Physics and Astronomy, Curtin University, Perth, WA 6102, Australia
[2] Department of Physics, Drake University, Des Moines, IA 50311, United States of America

E-mail: matthew.vaneck@student.curtin.edu.au

Received 13 September 2019, revised 15 October 2019
Accepted for publication 1 November 2019
Published 4 December 2019

Abstract

We applied the relativistic convergent close-coupling and the Dirac *B*-spline *R*-matrix methods to electron scattering from lead atoms. Differential and integrated cross sections are presented for elastic scattering and excitations from the ground state to the $6p7s$, $6p7p$, and $6p6d$ manifolds for energies ranging from 1 to 100 eV. The momentum-transfer, ionisation, and total scattering cross sections are also presented. Our results are compared with experimental data and previous theoretical predictions where available. Generally good agreement is found between the two theories and experiment, though some renormalisation of experiment is suggested.

Keywords: electron collisions, elastic scattering, electron impact excitation, cross section, ionisation, lead atom, resonance

(Some figures may appear in colour only in the online journal)

1. Introduction

Lead is a heavy, open-shell atom with two valence *p*-electrons above a mercury-like core. Its energy levels are strongly affected by relativistic effects, and the valence *p*-electrons introduce additional complexity when attempting an accurate description of the target structure. Modelling electron collisions with lead atoms is particularly challenging due to the strongly spin-dependent projectile-target interaction that significantly affects the collision dynamics. Accurate data for electron collisions with lead are important in applications. Plasma modelling requires a set of elastic and electron-impact excitation cross sections for a large number of reaction channels. In astrophysics, collision data play a critical role in the analysis of astrophysical spectra. These data are essential for identifying excitation lines and determining the chemical composition and abundances in stars and interstellar gas clouds, as well as testing models of nucleosynthesis [1–4].

There have been a number of experimental and theoretical studies of electron collisions with lead. Extensive angle-differential cross section (DCS) measurements were performed for elastic scattering by Tošić *et al* [5] and excitation of the $(6p7s)^3P_{0,1}$ states by Milisavljević *et al* [6, 7]. Elastic DCS were measured from 10 to 100 eV for scattering angles from 10° to 150°, while the DCS for excitation of the $(6p7s)^3P_{0,1}$ states were determined in the same energy range from 10 to 100 eV for scattering angles from 1° to 140°. Earlier DCS measurements of Williams and Trajmar [8] were performed at the single incident electron energy of 40 eV in the 10°–140° range for transitions comprising of elastic scattering and excitations of terms originating from the $6p^2$ configurations and the $(6p7s)^3P_1$ state. The absolute normalisation of the DCS was achieved by an extrapolation of the $(6p7s)^3P_1$ generalised oscillator strength (GOS) to the optical limit in the experiment of Williams and Trajmar [8], while Milisavljević *et al* [6, 7] used the forward scattering function (FSF) method [9]. Absolute normalisation of the DCS for elastic scattering and other excitations was obtained by cross normalisation to the $(6p7s)^3P_1$ DCS. Extrapolation to small and large scattering angles allowed the determination of angle-integrated cross sections (ICS) for elastic scattering and $(6p7s)^3P_1$ excitation.

Excitation of the $(6p7s)^3P_1$ state was studied using the relativistic distorted wave (RDW) method [6, 7]. The RDW calculations demonstrated generally good agreement with the experimental data reported in [6, 7], particularly at larger energies. However, at lower energies the RDW method is not expected to provide accurate results, and the agreement with the data of [6, 7] was particularly poor at the lowest measured energy of 10 eV. Note that the absolute DCS normalisation based on the FSF method used by [6, 7] becomes progressively less accurate as the incident electron energy decreases [10, 11].

Cross sections for elastic scattering were calculated by Tošić *et al* [5] in the relativistic model potential (RMP) approach by solving the Dirac equation for the projectile electron. Model potentials were used to describe the exchange, target polarisation, and coupling to inelastic channels. The dependence of the predicted cross sections on the target description with Hartree–Fock and Dirac–Fock wave functions was also tested. Given the approximations adopted in these calculations, the obtained results remained uncertain in the low- to intermediate-energy range. While the angular dependence of the elastic DCS was generally well reproduced, the agreement with available experiment for absolute values was mixed. This is not surprising, as the elastic cross section normalisation depends on the normalisation of the $(6p7s)^3P_1$ excitation, which in turn is not well established. A number of earlier calculations for elastic scattering adopting an approach similar to the RMP [5] were performed using the Kohn–Sham [12] and Dirac [13, 14] equations with results showing large variations in the calculated cross sections.

Dirac *R*-matrix calculations were carried out by Wijesundera *et al* [15] to obtain low-energy cross sections (up to 4 eV) for elastic scattering and excitation of the $(6p^2)^3P_1$ and $(6p^2)^3P_2$ states. The size of the close-coupling expansion was limited to the lowest five states (arising from the $6p^2$ configuration). Bartschat [16] used a similar 5-state close-coupling expansion in Breit–Pauli *R*-matrix (BPRM-5) to calculate elastic and inelastic cross sections up to 7 eV. More recently, the Dirac *B*-spline *R*-matrix method [17] employed a 31-state close-coupling expansion and presented elastic scattering cross sections up to 14 eV.

The most recent measurements of the ionisation cross sections for lead were performed more than twenty years ago by Freund *et al* [18] and McCartney *et al* [19], and the experimental data are in poor agreement with each other. The same is true for the earlier measurements of Golovach *et al* [20] and Pavlov and Stotskii [21]. Apart from the semi-empirical Lotz formula [22] and the semi-classical approach of Margreiter *et al* [23], the only quantum-mechanical estimate of the ionisation cross section is due to Jha and Roy [24] who used the binary encounter approximation (BEA). They found that the cross section is well described by ionisation from the $6p$ and $6s$ shells only, but agreement with experiment was poor.

The purpose of the present paper is to provide accurate cross sections for scattering of electrons with lead atoms in the ground state. We employ the relativistic convergent close-coupling (RCCC) method [25, 26] and the Dirac *B*-spline *R*-matrix method (DBSR) [17] to perform large-scale close-coupling calculations and establish convergent cross sections for elastic scattering, excitation of a number of low-lying levels (up to the $6p6d$ states), and single ionisation. Where available, we provide a detailed comparison with previous experimental and theoretical results and suggest a recommended cross section dataset. Unless specified otherwise, atomic units are used throughout this paper.

2. RCCC method

The detailed formulation of the RCCC method was presented in previous publications [25, 27], and hence only a brief overview is presented here. The bound spectrum of the lead atom is fairly well described by a model of two active electrons above a closed Dirac–Fock mercury-like core. The RCCC method was previously applied to a number of atoms that are well described by a similar model, including Hg [26, 28] and Yb [11]. The important difference is that the ground and excited states for Hg and Yb atoms are dominated by the singlet s^2 configuration and one-electron excitations from it, while for Pb the reference p^2 configuration leads to a significantly more complex spectrum that, however, is still dominated by one-electron excitations. The standard two-electron configuration-interaction technique [26, 29] is an effective method to obtain accurate wave functions and is well suited for the present case of the lead atom.

One-electron orbitals for the $s_{1/2}$ to $f_{7/2}$ symmetries are obtained by diagonalising the Dirac–Fock Hamiltonian of the Pb^+ quasi one-electron ion in a Sturmian (L-spinor) basis [30]. The Dirac–Fock core orbitals are obtained from the GRASP package [31]. Empirical one- and two-electron polarisation potentials are then used to account for the effects of the closed electron shells [32].

The static dipole polarisability of the Pb^{2+} core was chosen to be $\alpha_c = 13.3\ a_0^3$ ($a_0 = 0.529 \times 10^{-10}$ m denotes the Bohr radius), as recommended by Safronova *et al* [33] in agreement with the experimental value of Hanni *et al* [34]. The l-dependent fall-off radii of the one-electron polarisation potential (r_c^{pol}) were chosen to best represent the energy levels of the lead atom. We used 2.8, 3.3, 2.6 and 3.7 for $l = 0, 1, 2, 3$, respectively.

The length form of the optical oscillator strength (OOS) for the $(6p^2)\ ^3P_0 \rightarrow (6p7s)^3P_1$ transition was fitted to the value recommend by NIST, $f = 0.21$ [35], by choosing a two-electron polarisation potential fall-off radius of $r_c^{diel} = 3.5$. We found that the OOS is only weakly dependent on the fitting parameter r_c^{diel}. The OOS value obtained in the present calculations is $f = 0.205$. This is in a contrast to the situation for Hg or Yb where accounting for the two-electron polarisation potential leads to a reduction of the OOS for the resonance transition by nearly a factor of two.

To obtain an accurate representation of the Pb wave functions, the choice of two-electron configurations is particularly important. We adopted configurations of two types. The first set consists of $(6p_{1/2}\ nl_j)$ and $(6p_{3/2}\ nl_j)$ configurations, where (nl_j) span all one-electron orbitals. This set allows us to model high-lying excited states and provides a square-integrable representation of the target continuum. The second set consists of all $(nl_j,\ n'l'_{j'})$ configurations with one-electron orbitals limited to $6p_{1/2,3/2}$, $7s_{1/2}$, $7p_{1/2,3/2}$, and $6d_{3/2,5/2}$, $7d_{3/2,5/2}$, respectively. This set allows us to take

Table 1. Energies (in eV) of the lowest fifteen lead states obtained from the DBSR and RCCC models compared with the experimental results recommended by NIST [35].

Configuration	LS term	DBSR	RCCC	Experiment
$6p_{1/2}6p_{1/2}$	${}^3P_0$	0.00	0.00	0.00
$6p_{1/2}6p_{3/2}$	${}^3P_1$	0.98	0.90	0.97
$6p_{1/2}6p_{3/2}$	${}^3P_2$	1.35	1.29	1.32
$6p_{3/2}6p_{3/2}$	${}^1D_2$	2.63	2.63	2.66
$6p_{3/2}6p_{3/2}$	${}^1S_0$	3.69	3.78	3.65
$6p_{1/2}7s_{1/2}$	${}^3P_0^o$	4.37	4.35	4.33
$6p_{1/2}7s_{1/2}$	${}^3P_1^o$	4.41	4.38	4.38
$6p_{1/2}7p_{1/2}$	${}^3P_1$	5.31	5.32	5.32
$6p_{1/2}7p_{1/2}$	${}^3P_0$	5.53	5.52	5.51
$6p_{1/2}7p_{3/2}$	${}^3D_1$	5.54	5.53	5.54
$6p_{1/2}7p_{3/2}$	${}^3D_2$	5.56	5.55	5.56
$6p_{1/2}6d_{3/2}$	${}^3F_2^o$	5.60	5.59	5.63
$6p_{1/2}6d_{5/2}$	${}^3F_3^o$	5.72	5.72	5.74
$6p_{1/2}6d_{5/2}$	${}^3D_2^o$	5.68	5.70	5.71
$6p_{1/2}6d_{3/2}$	${}^3D_1^o$	5.69	5.71	5.71
Ionisation limit		7.32	7.38	7.42

Table 2. Oscillator strengths (length form) for the ground state of lead from the DBSR and RCCC models compared with available experimental or recommended values.

Transition	DBSR	RCCC	Experiment
$(6p^2)^3P_0 - (6p7s)^3P_1^o$	0.193	0.205	0.179 [35], 0.143 [36] 0.19 [37], 0.26 [1], 0.25 [38]
$(6p^2)^3P_0 - (6p6d)^3D_1^o$	0.499	0.545	0.31 [35], 0.869 [36], 0.35 [37]

into account electron–electron correlations that are particularly important for an accurate representation of the low-lying target states. Such a choice of two-electron configurations leads to a large number of target states ranging from states with total electronic angular momentum $J = 0$ to $J = 5$ of positive and negative parity. A comparison between the calculated and experimental energy levels for the lowest fifteen states is shown in table 1 and for the OOS in table 2.

For the lead atom, there are a number of experimental and theoretical values for the static dipole polarisability. Pershina *et al* [39] found a value of 46.96 a_0^3 using Dirac–Coulomb CCSD(T) calculations. Thierfelder *et al* [40] used all-electron relativistic coupled-cluster theory to determine a value of 47.3 a_0^3, in agreement with their experimental value of 47.1(7) a_0^3. We find that the RCCC value of 34.2 a_0^3 is systematically lower than the experimental or accurate theoretical results. This discrepancy is most likely due to the adoption of the frozen-core model, where inner core excitations are absent.

The calculated set of target states is used to expand the total scattering wave function and formulate a set of momentum-space close-coupling equations for the T-matrix elements. These equations are solved by standard techniques [25, 41], and scattering amplitudes, cross sections, and other collision parameters are obtained for the transitions of interest. Convergence of the scattering calculations was tested using a number of models of varying sizes. The first two models comprise only bound states, with 27 and 41 states, labelled as RCCC(27) and RCCC(41), respectively. The third model adds 34 continuum pseudostates with energies up to 1 eV (RCCC(75)), and the fourth and fifth add continuum pseudostates with energies up to 5 eV (RCCC(164)) and 10 eV (RCCC(295)). Two larger models were used to produce converged total ionisation cross sections. These models were built with one-electron orbitals extending to $h_{11/2}$ and include continuum pseudostates with energies up to 15 and 20 eV with total angular momenta up to $J = 7$. They were too large (up to 541 states) to be used in the RCCC calculations. Instead, we performed Born and unitarised Born calculations that were employed to extrapolate RCCC(295) cross sections.

3. *R*-matrix calculations

The R-matrix calculations for this work are based upon the DBSR method, which is an extension of the BSR approach [42] to the fully relativistic scheme. It was described in detail in its first applications to e−Cs collisions [17]. Subsequent applications to a variety of targets were reviewed in [43]. In particular, the DBSR code was already applied to the e−Pb problem, with emphasis on the study of the spin-asymmetry parameters [44, 45].

The distinguishing features of the (D)BSR method are (i) the ability to use term-dependent, and hence non-orthogonal, sets of one-electron orbitals (Dirac spinors in the present case) in the target description and (ii) B-splines as the underlying, effectively complete basis to expand the wave function of the projectile. Furthermore, it is an all-electron approach, and hence core-valence correlation effects can be described *ab initio*. As usual, the R-matrix method allows for an efficient calculation of results for a large number of collision energies, as needed particularly in near-threshold regimes that are often dominated by resonances.

An important aspect, especially for a complex target such as lead, is the structure description, which (as noted above) is by no means trivial. The target states in the present calculations were considered as a four-electron system above a closed $[1s^2 \ldots 5d^{10}]$ core. All calculations were completely *ab initio*, with the target states of Pb represented through B-spline box-based expansions of the form

$$\begin{aligned}\Phi(J\pi) = {} & \mathcal{A}\{\varphi(6s^26p, J')\cdot\phi(nlj)\}^J \\ & + \mathcal{A}\{\varphi(6s^27s, J')\cdot\phi(nlj)\}^J \\ & + \mathcal{A}\{\varphi(6s^26d, J')\cdot\phi(nlj)\}^J \\ & + \mathcal{A}\{\varphi(6s6p^2, J')\cdot\phi(nlj)\}^J \\ & + a\varphi(6s^26p^2, J) + b\varphi(6s6p^3, J). \qquad (1)\end{aligned}$$

Here $\mathcal{A}$ denotes the antisymmetrisation operator, J is the total electronic angular momentum of the target state, π is the parity, and all intermediate values J' and j were included. The wave functions for the Pb^+ states $\varphi(6s^2nl)$ and $\varphi(6s6p^2)$, as well as the wave functions for the equivalent-electron configurations $6s^26p^2$ and $6s6p^3$, were generated from separate Dirac–Fock calculations for each state, using the relativistic atomic structure package GRASP2K [46].

The unknown large and small radial components for the orbitals of the outer valence electron, $\phi(nlj)$, were expanded in separate B-spline bases. The coefficients of these expansions, together with the coefficients for the equivalent-electron configurations $6s^26p^2$ and $6s6p^3$, were found by diagonalising the Dirac–Coulomb Hamiltonian with the additional requirement that the wave functions vanish at the boundary. The above scheme allows us to account for the very strong configuration mixing between different $6pnl$ states, usually referred to as valence correlation. The scheme also includes the core-valence correlation related to the strong $6s$ to $6p$ excitation. The R-matrix radius was set to $50\,a_0$. We employed 111 B-splines of orders 8 and 9 for the large and small components of the spinors, respectively. The different B-spline orders for the two components ensure the absence of spurious solutions [47]. The relatively large number of splines is due to the fact that we employed a finite-size nuclear model with a Fermi nuclear potential [48].

Our scattering model includes 31 physical states of Pb, covering all states of the lowest $6p^2$, $6p7s$, $6p6d$, and $6p7p$ configurations, plus the ten $6s6p^3$ excited states. Note that the expansion (1) can be considered a model for the entire $6s^26pnl$ and $6s6p^2nl$ Rydberg series of the lead spectrum, including autoionising states and continuum pseudostates—if a sufficient number of terms are included. Although the DBSR approach can be set up in the R-matrix with pseudostates (RMPS) mode, the resulting continuum pseudospectrum is too rich and dense in the present case for our currently available computational resources. It would require thousands of pseudostates to cover even a small part of continuum. Such a task is not feasible at the present time. However, the accurate description of the target polarisation is of primary importance for elastic scattering at low energies. The full expansion (1) leads to a ground-state polarisability of $45.7\ a_0^3$, which is close to the experimental value $47.1(7)\ a_0^3$ [40]. The lowest 31 states provide only part of the total polarisability, $26\ a_0^3$. Adding the $6s6p^3$ states increases this value to $32\ a_0^3$. The remaining difference with the entire ground-state polarisability indicates the contributions of higher-lying bound states and the continuum spectrum of Pb, which are not included in the present model.

We calculated results for partial waves for total electronic angular momenta $J \leqslant 41/2$ numerically. This number is sufficient for electron energies below 20 eV. For higher energies, we employed a top-up procedure based on the Coulomb–Bethe approximation for dipole transitions or on the geometric-series approach for other transitions. The calculation in the external region was performed with the FARM programme [49]. Finally, the scattering amplitudes and the DCS were generated with the MJK programme [50].

As seen from table 1, the DBSR excitation energies agree with the NIST-recommended values up to deviations of 0.04 eV. This is considered a good agreement for fully *ab initio* calculations for such a heavy atom as Pb, when the target description needs to be used in a subsequent collision calculation with an additional projectile electron. It also indicates that the chosen model for the bound states of Pb contains all principal correlation corrections. The RCCC excitation energy levels are of the same accuracy as the DBSR results for all states, except for those arising from the $6p^2$ configurations where the RCCC results are marginally less accurate.

As mentioned in the previous section, the quality of the target description can be further assessed by comparing the results for the oscillator strengths of various transitions with experimental data and other theoretical predictions. Accurate oscillator strengths are very important to obtain reliable absolute values for the excitation cross sections, especially for optically allowed transitions at high electron energies. However, as seen from table 2, there are considerable discrepancies between the data reported from different measurements. Whereas, for the $(6p^2)\ ^3P_0 - (6p7s)\ ^3P_1$ transition, both DBSR and RCCC oscillator strengths are in reasonable agreement with the experimental values considering their spread, for the $(6p^2)\ ^3P_0 - (6p6d)\ ^3D_1$ transition the theoretical oscillator strengths considerably differ from all measurements. This raises questions regarding the uncertainties of the available experimental data. We note that the DBSR results obtained in the length and velocity forms of the electric dipole operator agree to better than 5% with each other. While this is not a guarantee for their accuracy, we consider this additional support for the near completeness of the DBSR expansions.

4. Results

The results of our calculations are presented below in the following order. We first present a comparison with available DCS and ICS experimental data and previous calculations for excitation of the $(6p7s)^3P_{0,1}$ states and elastic scattering. We then present ICS predictions for the states in the $6p7p$ and $6p6d$ manifolds ($(6p7p)^3P_{0,1}$, $(6p7p)^3D_{1,2}$, $(6p6d)^3F^o_{2,3}$, $(6p6d)^3D^o_{2,1}$), for which no previous experimental or theoretical results are available. Finally, we compare our results for the total ionisation cross sections with available experimental data and previous calculations.

4.1. Excitation of the 6p7s manifold

Angle-differential and angle-ICSs for electron impact excitation of the $(6p7s)\,^3P_{0,1}$ states were measured at low scattering angles (⩽10°) by Milisavljević *et al* [6] and intermediate scattering angles (10°–150°) by Milisavljević *et al* [7]. There are also 40 eV DCS measurements by Williams and Trajmar [8]. All DCS results are for the sum of the $(6p7s)^3P_0$ and $(6p7s)^3P_1$ states, as they were not experimentally distinguishable. The absolute normalisation of the cross sections was performed by extrapolation of the GOS to the optical limit by Williams and Trajmar [8] using the OOS value of 0.25 from

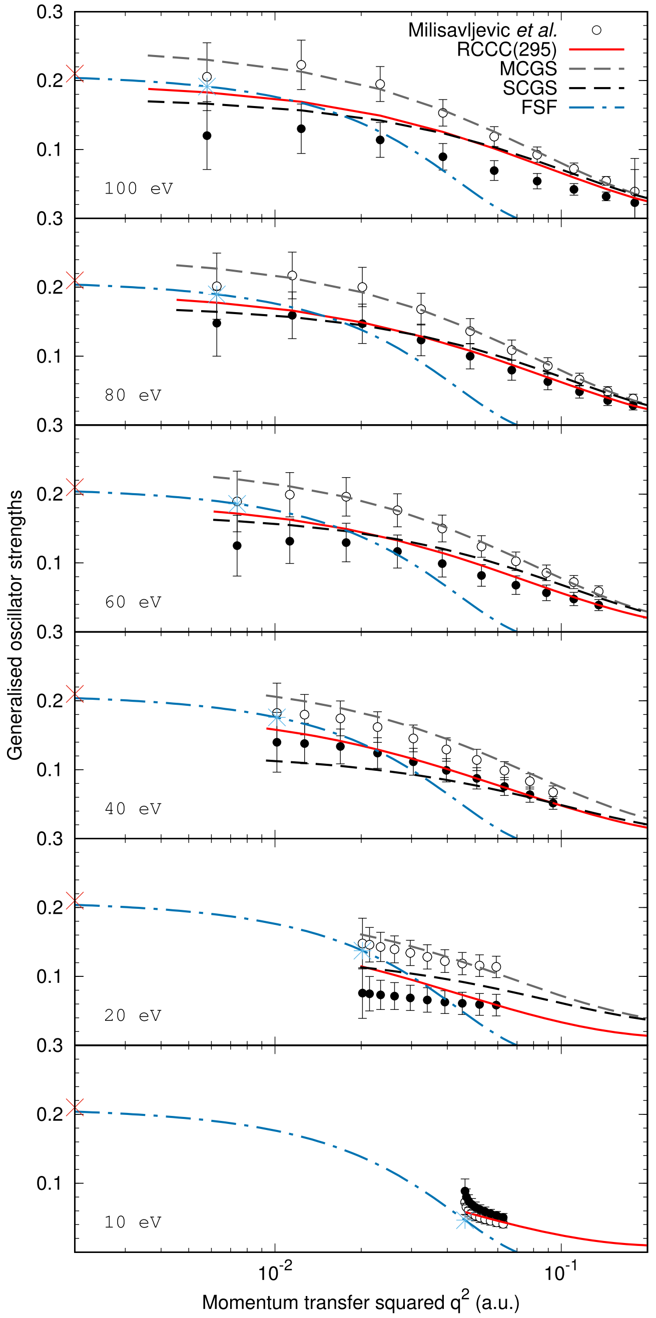

Figure 1. Generalised oscillator strengths for the $(6p7s)^3P_{0,1}$ states. The forward scattering function is presented with the optical oscillator strength of NIST [35]. The experimental data and the MCGS and SCGS calculations are from [6]. The filled circles indicate the experimental data renormalised at 10° for each energy.

Bell and King [38]. Milisavljević *et al* [7] used the FSF method [9] with an OOS value of 0.21. After extrapolation to small and large scattering angles, the angle-ICSs were produced. The measurements of Milisavljević *et al* [7] were accompanied by RDW calculations in two models, with a single-configuration (SCGS) description of the ground state and the $(6p7s)^3P_0$ states and a multi-configuration (MCGS) model that added configurations with $6d$ and $7p$ orbitals. The SCGS model yielded an OOS value of 0.168 and the MCGS model a larger value of 0.228.

Table 3. Calculated normalisation coefficients based on the experimental $(6p7s)^3P_1$ state GOS of Milisavljević *et al* [6] and the RCCC(295) model at 10°.

Energy	RCCC	Experiment	Factor
10 eV	0.050	0.041	1.225
20 eV	0.058	0.114	0.513
40 eV	0.052	0.067	0.767
60 eV	0.039	0.059	0.661
80 eV	0.028	0.038	0.734
100 eV	0.020	0.033	0.584

The experimental and calculated GOS of Milisavljević *et al* [6] are compared with the RCCC(295) calculations in figure 1. The MCGS and SCGS results are, respectively, larger and lower than the present RCCC(295) GOS predictions, as expected from the corresponding OOS values. The experimental GOS [6] are in reasonable agreement with the RCCC(295) GOS values, except for 20 eV where the normalisation procedure to FSF leads to a larger uncertainty.

In order to see the effect of normalisation of the experimental cross sections we renormalised the published experimental data [6, 7] to the RCCC(295) GOS values at 10°. The scaling factors for this change are shown in table 3 for each energy. The renormalised experimental data are shown as filled circles in figure 1. This renormalisation generally improves the agreement between RCCC(295) and experiment [6, 7]. However, it also highlights the differences in the small-angle analytical dependence, in particular at 20 eV where the slope of the experimental GOS is much flatter, and at 60, 80, and 100 eV, where the experimental small-angle GOS exhibit downward trends that are not seen in the RCCC(295) or RDW calculations.

In figure 2 we present DCS and in figure 3 ICS for excitation of the $(6p7s)^3P_{0,1}$ states. DBSR predicts slightly higher DCS values above 100° than RCCC at 10 and 20 eV. For 40 and 60 eV we see excellent agreement between the DBSR and RCCC results, with the DBSR calculations predicting slightly lower minima. For ICS, the DBSR cross sections are larger than those from RCCC below 40 eV, where the DBSR method also predicts noticeable resonance structure that is not reproduced in the RCCC results. The resonance behaviour close to the excitation threshold is quite typical and is usually present in both DBSR and RCCC calculations. More prominent resonances in the DBSR ICS are related to the $6s6p^3$ target states that are not included in the RCCC calculations. The larger ICS values in the DBSR model are mostly due to the lack of coupling to the higher excited states and the ionisation channels included in the RCCC calculations. This is illustrated in figure 4, where the convergence of the RCCC calculations is presented. The RCCC calculations converge at low energies to those obtained with the 41-state expansions, but at higher energies to the 295-state model.

The agreement between the RCCC results and experiment [6, 7] is good for the DCS in both the angular dependence and the absolute values, except for 20 eV where the experimental DCS absolute normalisation appears to be

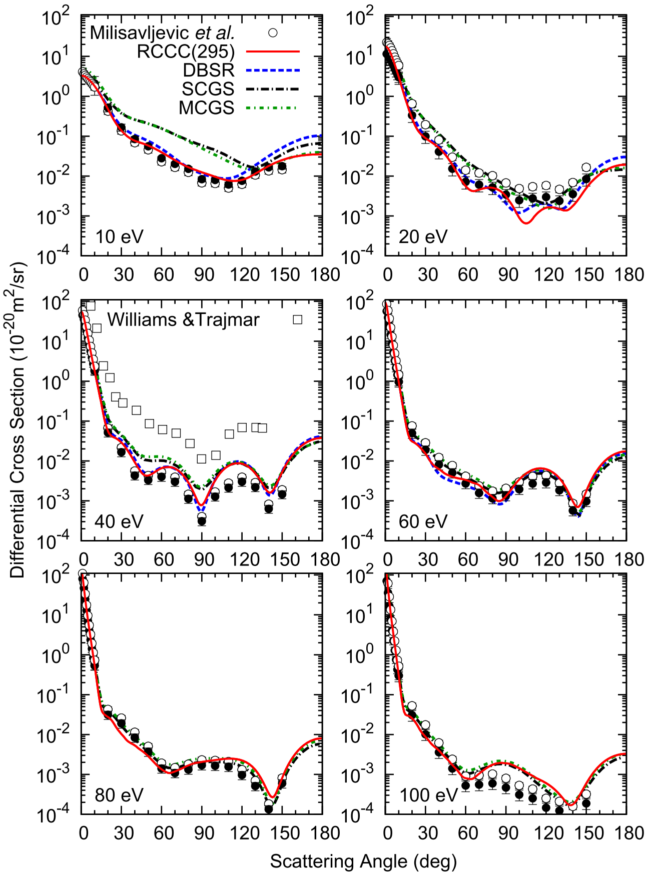

Figure 2. Differential cross sections (DCS) for excitation of the $(6p7s)^3P_{0,1}$ states. The present RCCC(295) and DBSR calculations are compared with the experimental data of Milisavljević *et al* [6, 7] and Williams and Trajmar [8], as well as RDW [7] calculations.

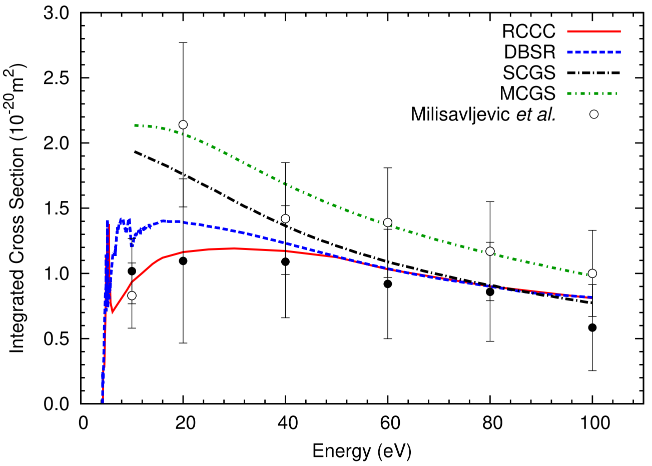

Figure 3. Integrated cross section (ICS) for excitation of the $(6p7s)^3P_{0,1}$ states. Theoretical and experimental results are as in figure 2.

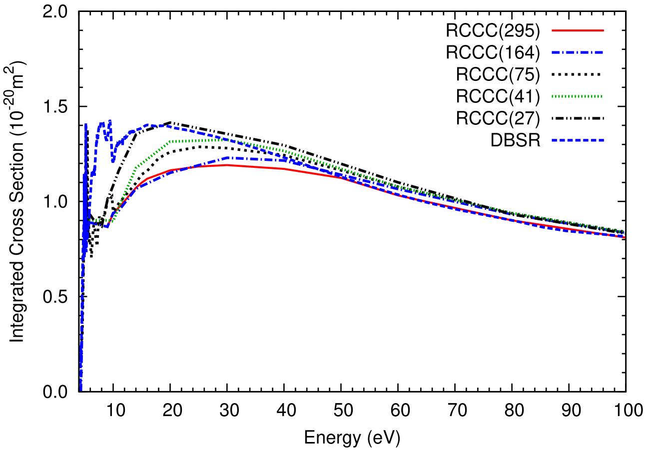

Figure 4. Convergence of the predicted angle-integrated cross section for excitation of the $(6p7s)^3P_{0,1}$ states.

too high. The RDW calculations are in good agreement regarding the energy dependence of the RCCC results and the experimental DCS above 40 eV, but they become progressively too large at intermediate scattering angles as the incident electron energy decreases. For the ICS, presented in figure 3, the supposedly more accurate MCGS model predicts substantially larger cross sections than RCCC and DBSR at all energies.

The renormalised experimental data provide a better fit at 10 and 20 eV incident energies, while they are very similar at higher energies. The difference in the angular dependence between the calculations and experiment shows that the fit is better for some angles and worse for others. For the ICS, the renormalised experimental data fit better with the flat energy dependence of the RCCC cross sections.

4.2. Elastic scattering cross sections

Elastic DCS for atomic lead were measured at 40 eV by Williams and Trajmar [8] and Marinković *et al* [51], and from 10 to 100 eV by Tošić *et al* [5]. Calculations of elastic scattering using a single-channel (essentially potential scattering) approach were reported in a number of publications [5, 12–14]. In these calculations, the Dirac or Kohn–Sham equations were solved for the projectile electron with various choice of model potentials that can only be justified at high energies. We compare in more detail with the recent RMP calculations of Tošić *et al* [5] that were performed with the target wave functions description obtained in the Hartree–Fock and Dirac–Fock formulations.

In figure 5 we present a comparison of the present RCCC (295) and DBSR elastic DCS with available experimental and theoretical elastic DCS. The RCCC and DBSR models are in good agreement at 20, 40, and 60 eV, while at 10 eV some differences are apparent above 90°. The agreement between the RCCC and DBSR results is consistently much closer than with the RMP calculations of Tošić *et al* [5].

The experimental DCS results of Tošić *et al* [5] for elastic scattering were normalised based on the elastic-inelastic ratio and the absolute normalisation of Milisavljević *et al* [7] for the excitation cross sections of the combined $(6p7s)^3P_{0,1}$ states. Accordingly, we rescaled them with the same factor and present the renormalised experiment as filled circles. Generally, there is qualitative agreement of the RCCC and DBSR elastic cross sections with the angular dependence

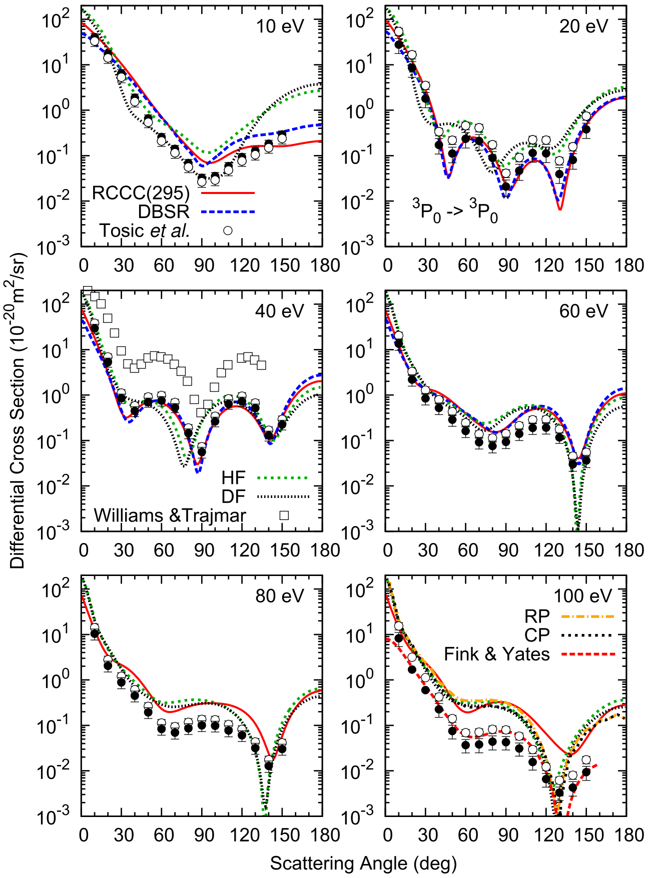

Figure 5. Differential cross sections for elastic scattering. The present calculations performed with the RCCC(295) and DBSR models are compared with the experimental data of Tošić *et al* [5] and Williams and Trajmar [8] and with the RMP calculations of [5] performed in the HF and DF models. In the 100 eV panel, the RP and CP calculations of Kumar *et al* [13] are presented along with the calculations of Fink and Yates [14]. The filled circles indicate the renormalised experimental data (see text).

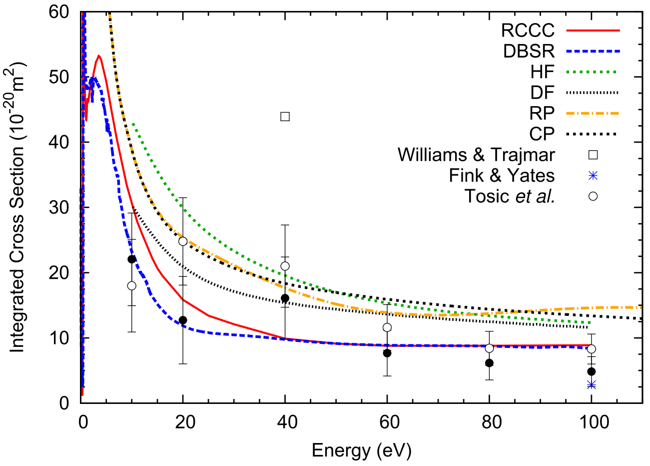

Figure 6. Integrated cross sections for elastic scattering. Experiment and calculations are labelled as in figure 5.

of the measured DCS [51], but the absolute values differ significantly. This is most likely related to the normalisation procedure adopted to put the experimental data on the absolute scale. The difficulty in absolute normalisation is particularly apparent for the 40eV elastic DCS of Williams and Trajmar [8], which are significantly larger compared to other measurements and calculations, whereas the agreement in angular dependence is good. While the renormalised experiment of Tošić *et al* [5] is closer to the calculations in the 10–40 eV range, it gives worse agreement at larger energies. At these high energies, there is agreement with the published and the renormalised experimental data at small angles, but the agreement becomes increasingly worse at larger angles, where the original data are closer to our calculations. This indicates that simple rescaling will not achieve agreement between experiment and theory at all angles. At 100 eV the calculations of Fink and Yates [14] are in good agreement with the renormalised experimental data below 30° and with the published data above this, although it predicts a much deeper minimum at 130°. The real-potential (RP) and complex potential (CP) calculations of Kumar *et al* [13] are in agreement with the calculations of Tošić *et al* [5] and only differ above 150° where they predict smaller cross sections.

In figure 6, we present elastic ICS using the RCCC and DBSR models, with a comparison to previous theory and experiment. The RCCC curve is a combination of the RCCC (295) model above 4 eV and the RCCC(27) model at lower energies. Both the RCCC and DBSR methods predict a large maximum at about 3 eV. The DBSR predictions converge towards the RCCC results above 40 eV. At lower energies the small but systematic difference between the RCCC and the DBSR cross sections comes from the forward scattering where the DBSR DCS are lower than the RCCC values as can be seen from figure 5. This is consistent with the lack of reaction channels for high excited states and 6*p* ionisation in the DBSR model compared to RCCC that typically leads to lower cross sections in the former. We find poor agreement with the RMP results [5] that predict a similar ICS energy dependence for both HF and DF models in the 10–100 eV region, but are systematically larger compared to the present RCCC and DBSR cross sections. The RP and CP calculations of Kumar *et al* [13] are similar across the energy range, and predict ICS in between the HF and DF models of Tošić *et al* [5]. The experimental ICS were obtained from the measured DCS by extrapolating to small and large scattering angles before integrating. Our results agree with experiment only at higher energies, 60 eV and above, and predict a very different ICS energy dependence. However, renormalising the experiment yields improved agreement across the entire energy range.

The momentum-transfer cross sections (MTCS) for elastic scattering are presented in figure 7 for the RCCC and DBSR models. These are compared with the RMP calculations and the experimental data of Tošić *et al* [5]. Good agreement with the RMP theory is found at 40 eV and above, and both RCCC and DBSR show good agreement and model the experimental energy dependence fairly well. The calculations of Kumar *et al* [13] are again similar across the energy range and predict larger ICS than the experiment or other calculations. The better agreement of the RCCC result with experiment [5] for the MTCS than for the ICS suggests that the significant differences between the RCCC

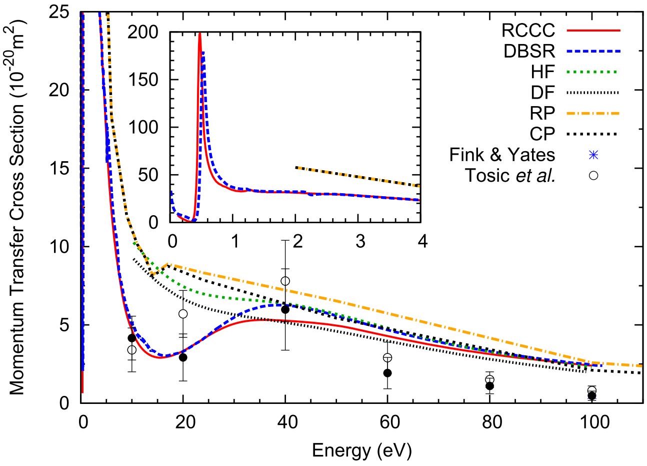

Figure 7. Momentum transfer cross section for elastic scattering. The inset figure shows the peak at 0.6 eV for both RCCC and DBSR models. Experiment and calculations are labelled as in figures 5 and 6.

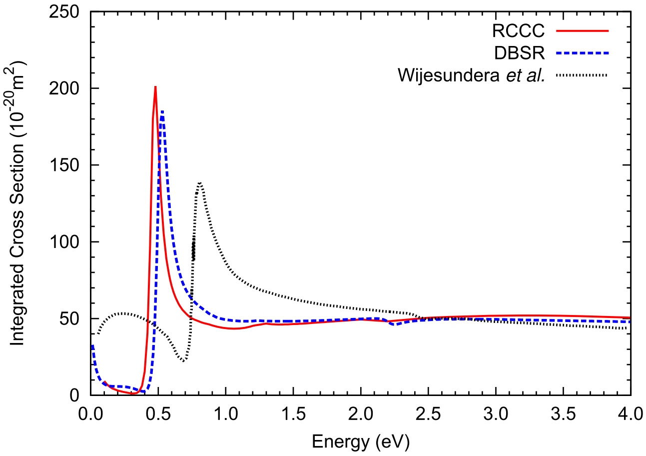

Figure 9. Integrated cross section for elastic scattering at low energies between 0 and 4 eV, as obtained in the RCCC(27) and DBSR models. Also shown are the calculations by Wijesundera *et al* [15].

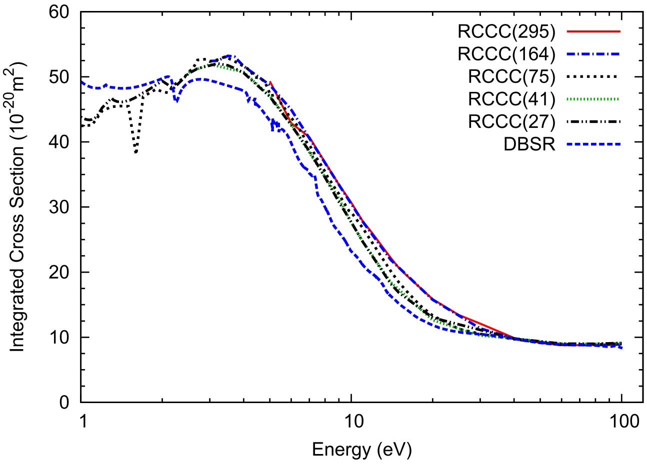

Figure 8. Convergence of the predicted angle-integrated cross sections for elastic scattering. RCCC(164) is only shown above 3 eV and RCCC(295) is only shown above 5 eV.

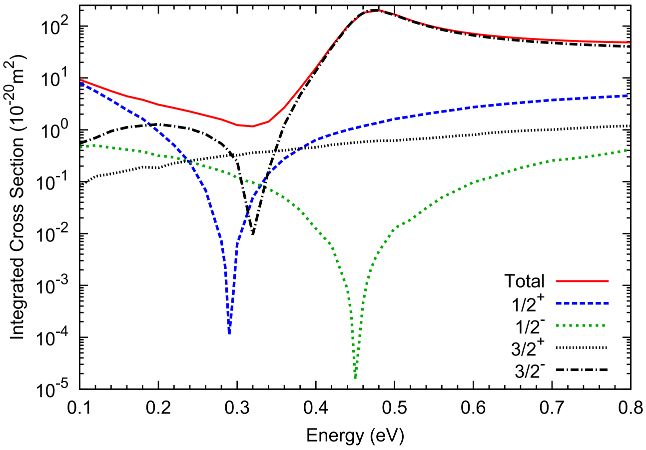

Figure 10. Partial-wave and summed integrated cross section for elastic scattering at low energies between 0.1 and 0.8 eV as obtained in the RCCC(27) model.

and experimental ICS originate from small scattering angles, as they are suppressed in producing the MTCS from the DCS. Renormalising the experiment gives better agreement up to 40 eV, but does not have much effect at the higher energies.

We demonstrate the convergence of the RCCC calculations in figure 8. The two largest RCCC models, RCCC(295) and RCCC(164), show good agreement and converge to the results from the smaller models below 10 eV. The smaller-size RCCC models agree well with DBSR above the ionisation threshold. The 75-state model is clearly converged at low energies (4 eV and below). The DBSR calculations show a resonance behaviour at about 2.5 eV, which also appears in the RCCC calculations.

The low-energy elastic ICS are presented in figure 9. Here the RCCC(27), DBSR, and the 5-state model of Wijesundera *et al* [15] predict a sharp resonance. This resonance occurs in the p-wave, and its location is very sensitive to the calculation details. The present RCCC and DBSR results are in close agreement regarding the position of the resonance. Even though both present RCCC and DBSR models do not reproduce the polarisability to the full extent, we believe that the results are close to convergence. We present a partial wave decomposition of this angle-ICS for the energy range 0.1–0.8 eV in figure 10. The s-wave partial cross section (total $J = 1/2$, even parity, labelled $1/2^+$) shows a typical Ramsauer–Townsend minimum at 0.29 eV. However, as other partial waves are not small at this energy, the summed ICS does not show such a sharp minimum. Above 0.2 eV the elastic cross section is dominated by the projectile p-wave ($3/2^+$) with the resonance at 0.47 eV.

4.3. Excitation of the 6p6d *and* 6p7p *manifolds*

The OOS for the $(6p^2)^3P_0 \rightarrow (6p6d)^3D_1^{\rm o}$ transition is more than twice that for the $(6p^2)^3P_0 \rightarrow (6p7s)^3P_1^{\rm o}$ transition. This suggests that the excitation cross sections for the $(6p6d)^3D_1^{\rm o}$ state should be at least as large as for the $(6p7s)^3P_1^{\rm o}$ state. Indeed, the large peak for the $(6p6d)^3D_1^{\rm o}$ state can clearly be seen in the energy loss spectrum of lead presented by

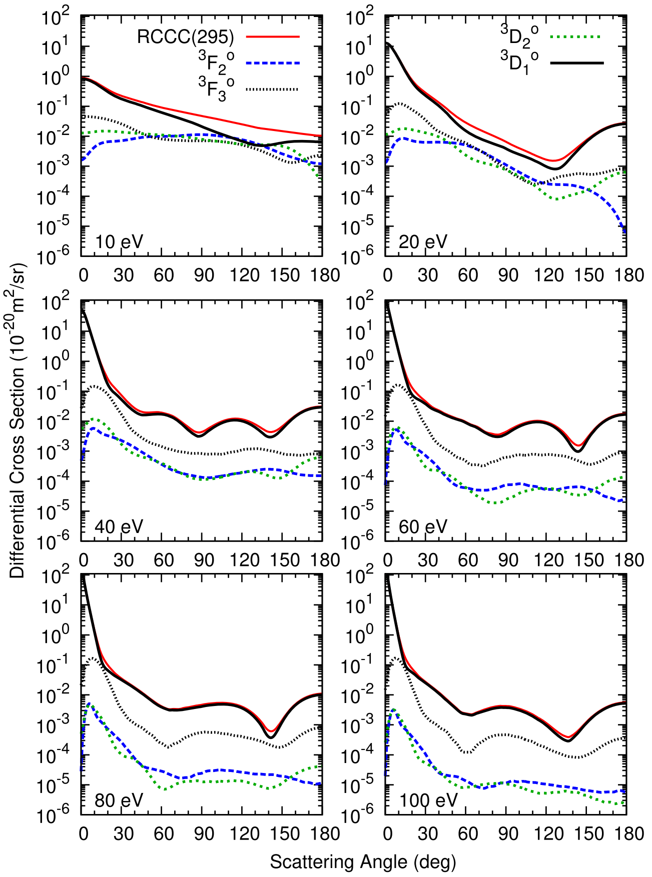

Figure 11. Differential cross sections for excitation of the 6*p*6*d* manifold. The summed and selected individual cross sections are shown.

Milisavljević *et al* [7]. The energy resolution of the DCS measurements reported by Milisavljević *et al* [7] is 0.12 eV. Since the 6*p*7*p* states lie about 0.3 eV lower than the 6*p*6*d* states, the energy-loss spectrum signals from these two manifolds partially overlap. We present in figures 11–14 the DCS and ICS for the states in the 6*p*6*d* and 6*p*7*p* manifolds. No other theoretical or experimental results are available for comparison. The large differences between the RCCC and DBSR calculations seen in figures 12–14 are somewhat expected, as the DBSR model neither accounts for coupling to the high-lying excited states nor to the direct ionisation channels. The convergence of the RCCC calculations is slower for the 6*p*6*d* cross sections than for the 6*p*7*s* cross sections, but it is clearly achieved with the RCCC(295) model. The smaller RCCC(27) model follows the DBSR results more closely.

The RCCC and DBSR calculations predict a very different energy dependence of the cross sections for the 6*p*6*d* and 6*p*7*p* manifolds. The dipole-allowed excitation of the $(6p6d)^3D_1^o$ state is dominant among the states in the 6*p*6*d* and 6*p*7*p* manifolds. This cross section rises slowly from threshold and exhibits a broad maximum around 50 eV with the typical energy dependence for dipole-allowed transitions. The 6*p*7*p* cross section shows a sharp rise at the threshold, followed by a slow decrease with the typical energy dependence for dipole-forbidden transitions.

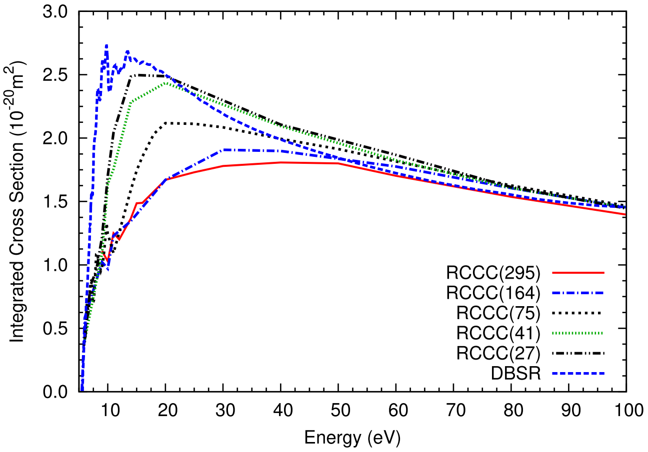

Figure 12. Convergence of the predicted ICS for excitation of the 6*p*6*d* manifold.

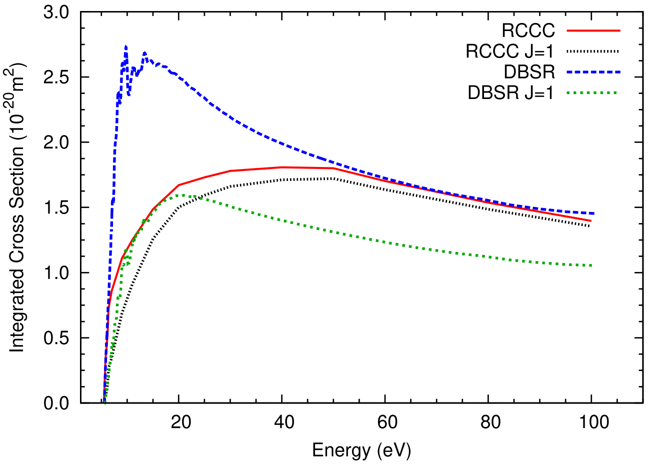

Figure 13. Integrated cross sections for scattering excitation of the 6*p*6*d* manifold, as calculated with the RCCC(295) model. The dominant contribution from the $J = 1$ state is also shown individually for both the DBSR and RCCC calculations.

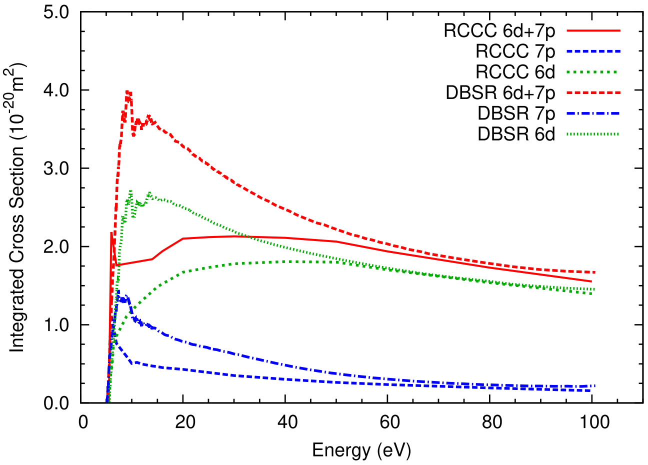

Figure 14. ICS for the 6*p*7*p* manifold and summed with the 6*p*6*d* manifold.

4.4. Total ionisation cross section

The total cross sections (TCSs) for electron impact ionisation of lead were measured by Freund *et al* [18] and McCartney *et al* [19]. There are also older measurements by Golovach *et al* [20] and Pavlov and Stotskii [21]. The agreement between these measurements is poor. Jha and Roy [24] performed calculations in the BEA to analyse the contributions of the various subshells. For single ionisation, they found that investigating the 6*s* and 6*p* subshells is sufficient. Kim and Stone [52] performed calculations employing the similar binary encounter Bethe (BEB) method, but they also included the contribution from excitation-autoionisation.

We calculated the cross sections for ionisation of the 6*p* electrons using the RCCC(295) model. ionisation of a 6*p* electron provides the dominant contribution to the single ionisation cross section from threshold at 7.42 eV to about 15 eV. At larger energies, ionisation of the 6*s* electron starts to contribute. To obtain the single ionisation cross section we first determined our best estimate of the 6*p* ionisation from the RCCC calculations and then summed it with the cross sections for 6*s* ionisation calculated in the RCCC method and excitation-autoionisation cross sections calculated with the DBSR method.

Ionisation of *p*-electrons leads to ejected electrons with a larger orbital angular momentum than in the more common case of ionisation of *s*-electrons. Therefore, a larger expansion is required to model the ionisation process in the close-coupling method, though this is constrained by unitarity [53]. The RCCC(295) model includes one-electron orbitals up to $f_{7/2}$, target pseudostates with maximum angular momentum $J = 5$, and energies up to 10 eV. This should be sufficient to describe the major ionisation channels up to 15 eV incident electron energies.

At larger energies, orbitals with a larger orbital angular momentum and pseudostates with larger angular momentum and energies are required. Full close-coupling calculations are too computationally expensive in this case, and hence we adopt an extrapolation technique to estimate the ionisation cross section. This technique relies on performing calculations in a large first-Born approximation (FBA) or unitarised-Born approximation (UBA) and then using the ratio of the first-order results with the RCCC calculation to extrapolate the RCCC(295) ionisation cross sections. In the present paper, we used the UBA ratios for extrapolation. We find that convergence in the first-order results is achieved with the one-electron expansion up to $f_{7/2}$ orbitals and target pseudostates with maximum angular momentum $J = 5$ and energies up to 20 eV. This leads to a total of 541 states. In figure 15 we present the RCCC(295) 6*p* ionisation cross sections together with the FBA and UBA results for 295- and 541-state expansions. The extrapolation procedure is required only at incident electron energies from 15 to 100 eV. Below 15 eV the RCCC(295) model is sufficiently accurate, while above 100 eV the UBA calculations provide a good estimate.

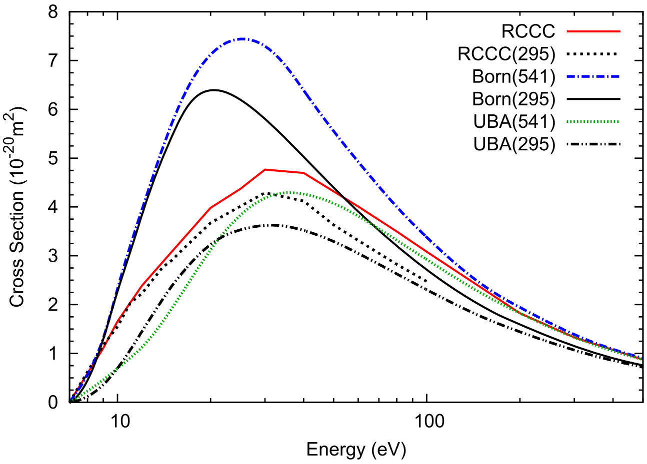

Figure 15. Cross section for electron impact single ionisation of the Pb ground state. The RCCC calculations are for the outermost valence subshell (6*p*) only. The RCCC(295) calculations were extrapolated using the ratio of UBA results.

The threshold for ionisation from the $6s^2$ shell is 14.9 eV. The RCCC method allows for an estimate for the 6*s* ionisation cross section by treating the $6p^2$ electrons as inert. The $^3P_0$ ground state of Pb has the leading configuration $6s^26p^2_{1/2}$ with a mixing coefficient 0.96, as obtained, for example, by Milisavljević *et al* [6] when performing Dirac–Fock calculations using the GRASP programme [31]. The two $6p_{1/2}$ electrons form a closed shell, and the RCCC calculations can be carried out by allowing excitations from the active $6s^2$ shell. Such calculations were performed using the RCCC approach in a model that contained 296 states with maximum angular momentum $J = 7$ and an underlying L-spinor basis extending to $i_{13/2}$. The same extrapolation process as used for the 6*p* ionisation was employed to construct the 6*s* ionisation cross section.

In figure 16 we present the 6*s*, 6*p*, and excitation -autoionisation components of the single ionisation cross section, as calculated by the present RCCC and DBSR methods. These results are compared with the BEA predictions of Jha and Roy [24] and the BEB calculations of Kim and Stone [52]. The BEB calculations were presented in [52] as summed over the 6*s* and 6*p* components. Using the details given in [52], we calculated the separate 6*s* and 6*p* cross sections presented here. We see generally good agreement between our results and the BEB cross sections of Kim and Stone [52] for the 6*p* component. Both the RCCC and BEB 6*p* cross section are systematically smaller than the BEA cross sections of Jha and Roy [24], with the cross-section maximum smaller by approximately 30% and the peak shifted towards higher energies compared to the BEA results (from 20 to 35 eV).

We see good agreement in the predicted energy dependence of 6*s* ionisation for the RCCC and BEB cross sections, but the RCCC results lie systematically below the BEB cross sections. Both the RCCC results and BEB cross sections are significantly smaller than the BEA cross sections (by more than a factor of two) and show the peak at higher energy compared to the BEA results.

For excitation-autoionisation, we see good agreement between the DBSR and estimates of Kim and Stone [52]. The latter were obtained from the scaled FBA calculations (as developed by Kim [54]) for the excitations of the autoionising levels calculated in a single-configuration Dirac–Fock

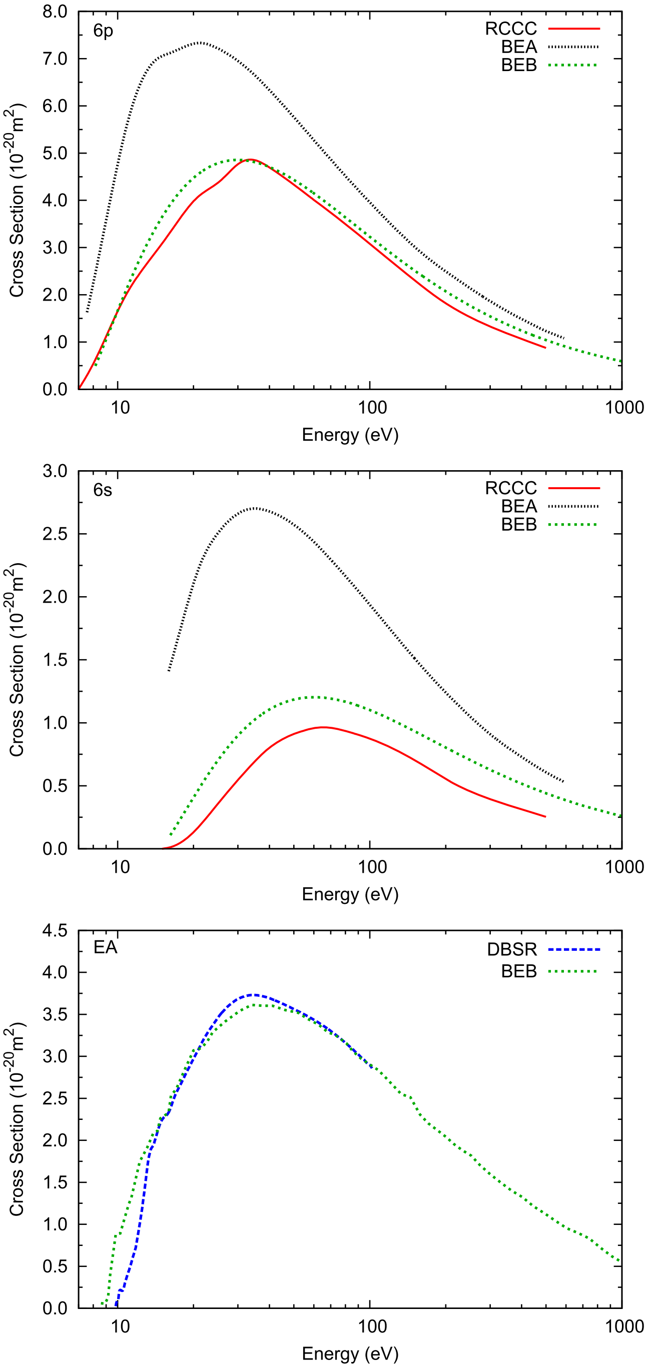

Figure 16. Components of the cross section for electron impact single ionisation of the Pb ground state. The present RCCC predictions for the 6p and 6s ionisation and DBSR predictions for the excitation-autoionisation (EA) are compared with the BEA calculations of Jha and Roy [24] and the BEB and EA results of Kim and Stone [52].

approach. The present and [52] excitation-autoionisation cross sections have a similar peak energy at 35 eV and a peak magnitude, where the DBSR prediction is only marginally larger. Both methods have nearly identical results above 50 eV. Below 15 eV, however, we see a sharper rise in the DBSR calculation, with smaller numbers than in the BEB model.

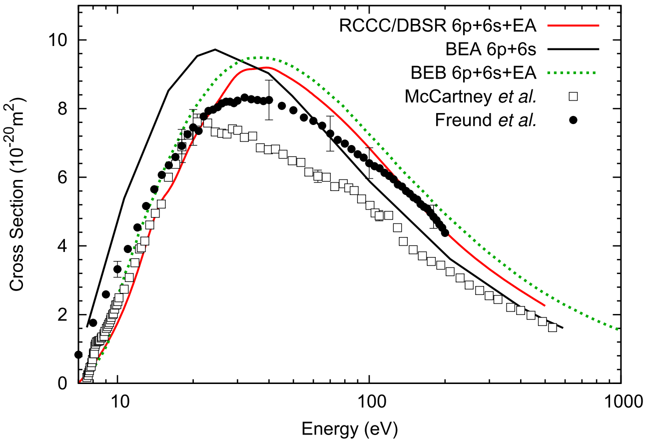

Figure 17. Cross section for electron impact single ionisation of the Pb ground state. The present RCCC/DBSR predictions are compared with the experimental data of Freund *et al* [18] and McCartney *et al* [19], the BEA calculations of Jha and Roy [24], and the BEB results of Kim and Stone [52]. Sample error bars are shown at various energies.

The excitation-autoionisation processes provide a relatively large contribution to the ionisation. Kim and Stone [52] were concerned with the reliability of their calculations due to a possible breakdown of the scaling procedure or an insufficient accuracy of the wave functions for the autoionising levels. However, a more accurate treatment of these aspects in the DBSR calculations led to practically the same results.

In figure 17 we present the measured single ionisation cross sections of Freund *et al* [18] and McCartney *et al* [19] as well as the results of calculations by Jha and Roy [24] and Kim and Stone [52] for ionisation from the summed 6s plus 6p subshells, together with the present RCCC/DBSR estimate for single ionisation. For the present results and the BEB calculations [52], the excitation-autoionisation component is also included. There is reasonable agreement in the energy dependence between our results and those of Kim and Stone [52] across the common range of energies, but their cross sections are systematically larger above 10 eV. Below 30 eV, the BEA results are higher than experiment and other calculations. Above this energy they drop below our results to be in line with the experimental data of McCartney *et al* [19] above 400 eV.

At large energies, the present RCCC/DBSR estimate for single ionisation is in better agreement with the measurements of Freund *et al* [18], showing the maximum of the cross section at the same energy of 30 eV. For this peak range from 20 to 100 eV, the RCCC/DBSR results are higher than the data from this experiment. The measurements of McCartney *et al* [19] are lower than the RCCC/DBSR estimate above energies of 20 eV. At energies below 30 eV, the RCCC/DBSR cross section lies in between the measurements, and below those of McCartney *et al* [19] below 10 eV. Below 15 eV the single ionisation cross section is dominated by ionisation of the 6p electrons.

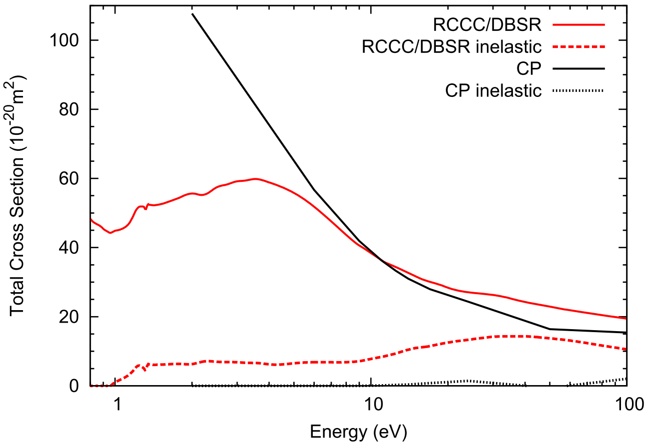

Figure 18. Total and inelastic cross section (TCS). Present calculations performed with the RCCC and DBSR models are compared with the CP calculations of Kumar *et al* [13].

4.5. Total and inelastic cross sections

We present the TCS and total inelastic cross section in figure 18. After adjusting for correct thresholds we find that RCCC and DBSR total inelastic cross sections are practically the same at low energies. The RCCC/DBSR estimate for the total inelastic cross section is produced in the following way. Below 4 eV we have used the RCCC(27) model, while above 4 eV we have used the RCCC(295) model without the ionisation contribution, to which we added the RCCC estimate of 6*s* and 6*p* ionisation and the DBSR estimate of excitation-autoionisation as in figure 17. The TCS is then obtained by summing the RCCC/DBSR estimate of the total inelastic cross section with the RCCC elastic cross section. The TCS results obtained in the CP model of Kumar *et al* [13] are lower than the present results above 10 eV but significantly larger at low energies. From presented TCS and elastic cross sections by Kumar *et al* [13] we have obtained the total inelastic cross section that is also presented in figure 18. These CP results are significantly lower than the RCCC/DBSR total inelastic cross section at all energies.

5. Summary and conclusions

We presented cross sections for the major reaction channels in electron collisions with lead atoms obtained using RCCC and DBSR methods. These include cross sections for elastic scattering and excitation of the $6p7s$, $6p7p$ and $6p6d$ manifolds from the $(6p^2)^3P_0$ ground state. We compared our results with the experimental data of Tošić *et al* [5] for elastic scattering and of Milisavljević *et al* [6, 7] for excitation of the $(6p7s)^3P_{0,1}$ states, as well as RMP [5] and RDW calculations [6, 7]. We find generally good agreement with experiment regarding the angular dependence of the DCSs, whereas the agreement for the absolute values was mixed. The latter often lead to rather poor agreement with published experimental values for the angle-ICSs. After renormalising the experimental data of Milisavljević *et al* [6, 7] and Tošić *et al* [5], we find similar agreement for the DCSs, but a definite improvement in both the energy dependence and the absolute values of the angle-ICSs.

We also presented RCCC estimates for the one-electron ionisation cross sections from both the 6*s* and 6*p* subshells, as well as DBSR estimates for excitation-autoionisation processes. The resulting RCCC/DBSR estimates of the total one-electron ionisation cross section are in overall best agreement with the measurements of Freund *et al* [18] and the BEB calculations of Kim and Stone [52]. Finally, combining the RCCC and DBSR results we have obtained an estimate for the total scattering cross section. We hope that the presented cross sections will be useful in various modelling applications in plasma and astrophysics. Our results are available in electronic form upon request.

Acknowledgments

The work of MvE, DVF, and IB was supported by the Australian Research Council and resources provided by the Pawsey Supercomputing Centre with funding from the Australian Government and the Government of Western Australia. OZ and KB acknowledge support from the United States National Science Foundation under grants No. PHY-1520970, PHY-1803844, and OAC-1834740, as well as supercomputer resources through the XSEDE allocation PHY-090031.

ORCID iDs

Matthew P van Eck https://orcid.org/0000-0001-5161-8263
Igor Bray https://orcid.org/0000-0001-7554-8044
Klaus Bartschat https://orcid.org/0000-0001-6215-5014

References

[1] Biémont E, Garnir H P, Palmeri P, Li Z S and Svanberg S 2000 *Mon. Not. R. Astron. Soc.* **312** 116
[2] Cowan J J, Sneden C, Truran J W and Burris D L 1996 *Astrophys. J. Lett.* **460** L115
[3] Goswami A, Aoki W, Beers T C, Christlieb N, Norris J E, Ryan S G and Tsangarides S 2006 *Mon. Not. R. Astron. Soc.* **372** 343
[4] Cardelli J 1994 *Science* **265** 209–13
[5] Tošić S D, Rabasović M S, Šević D, Pejčev V, Filipović D M, Sharma L, Tripathi A N, Srivastava R and Marinković B P 2008 *Phys. Rev.* A **77** 012725
[6] Milisavljević S, Rabasović M S, Šević D, Pejčev V, Filipović D M, Sharma L, Srivastava R, Stauffer A D and Marinković B P 2007 *Phys. Rev.* A **75** 052713
[7] Milisavljević S, Rabasović M S, Šević D, Pejčev V, Filipović D M, Sharma L, Srivastava R, Stauffer A D and Marinković B P 2007 *Phys. Rev.* A **76** 022714
[8] Williams W and Trajmar S 1975 *J. Phys. B: At. Mol. Phys.* **8** L50
[9] Avdonina N B, Felfli Z and Msezane A Z 1997 *J. Phys. B: At. Mol. Opt. Phys.* **30** 2591
[10] Fursa D V and Bray I 1999 *Phys. Rev.* A **59** 282
[11] Bostock C J, Fursa D V and Bray I 2011 *Phys. Rev.* A **83** 052710

[12] Geesmann H, Bartsch M, Hanne G F and Kessler J 1991 *J. Phys. B: At. Mol. Opt. Phys.* **24** 2817
[13] Kumar P, Jain A K, Tripathi A N and Nahar S N 1994 *Phys. Rev.* A **49** 899
[14] Fink M and Yates A C 1970 *At. Data* **1** 385
[15] Wijesundera W P, Grant I P and Norrington P H 1992 *J. Phys. B: At. Mol. Opt. Phys.* **25** 2165
[16] Bartschat K 1985 *J. Phys. B: At. Mol. Phys.* **18** 2519
[17] Zatsarinny O and Bartschat K 2008 *Phys. Rev.* A **77** 062701
[18] Freund R S, Wetzel R C, Shul R J and Hayes T R 1990 *Phys. Rev. A* **41** 3575
[19] McCartney P C E, Shah M B, Geddes J and Gilbody H B 1998 *J. Phys. B: At. Mol. Opt. Phys.* **31** 4821
[20] Golovach D G, Drozdov A N, Rakhovskii V I and Shustryakov V M 1987 *Meas. Techn. USSR* **30** 587
[21] Pavlov S I and Stotskii G I 1970 *Sov. Phys. JETP* **31** 61
[22] Lotz W 1967 *Z. Phys.* **206** 205
[23] Margreiter D, Deutsch H and Märk T 1994 *Int. J. Mass Spectrom. Ion Process.* **139** 127
[24] Jha L K and Roy B N 2004 *Eur. Phys. J.* D **29** 313
[25] Fursa D V and Bray I 2008 *Phys. Rev. Lett.* **100** 113201
[26] Bostock C J, Fursa D V and Bray I 2010 *Phys. Rev.* A **82** 022713
[27] Bostock C J 2011 *J. Phys. B: At. Mol. Opt. Phys.* **44** 083001
[28] Bostock C J, Fursa D V and Bray I 2012 *Phys. Rev.* A **85** 062707
[29] Fursa D V and Bray I 1995 *Phys. Rev.* A **52** 1279
[30] Grant I P and Quiney H M 2000 *Phys. Rev.* A **62** 022508
[31] Dyall K, Grant I, Johnson C, Parpia F and Plummer E 1989 *Comput. Phys. Commun.* **55** 425
[32] Fursa D V and Bray I 1997 *J. Phys. B: At. Mol. Opt. Phys.* **30** 5895
[33] Safronova M S, Kozlov M G and Safronova U I 2012 *Phys. Rev.* A **85** 012507
[34] Hanni M E, Keele J A, Lundeen S R, Fehrenbach C W and Sturrus W G 2010 *Phys. Rev.* A **81** 042512
[35] Kramida A, Ralchenko Y, Reader J and (NIST ASD Team) 2018 *NIST Atomic Spectra Database* (Gaithersburg, MD: National Institute of Standards and Technology) (ver. 5.5.6) (https://physics.nist.gov/asd) (Accessed: 30 August 2018)
[36] Morton D C 2000 *Astrophys. J. Suppl. Ser.* **130** 403
[37] Doidge P 1995 *Spectrochim. Acta* B **50** 209
[38] Bell G D and King R B 1961 *Astrophys. J.* **133** 7181
[39] Pershina V, Borschevsky A, Eliav E and Kaldor U 2008 *J. Chem. Phys.* **128** 024707
[40] Thierfelder C, Assadollahzadeh B, Schwerdtfeger P, Schäfer S and Schäfer R 2008 *Phys. Rev.* A **78** 052506
[41] Bray I and Stelbovics A T 1992 *Phys. Rev.* A **46** 6995
[42] Zatsarinny O 2006 *Comput. Phys. Commun.* **174** 273
[43] Zatsarinny O and Bartschat K 2013 *J. Phys. B: At. Mol. Opt. Phys.* **46** 112001
[44] Hamelbeck V, Hanne G F, Zatsarinny O, Bartschat K, Gangwar R K and Srivastava R 2009 *Phys. Rev.* A **80** 062711
[45] Zatsarinny O, Wang Y and Bartschat K 2013 *J. Phys. B: At. Mol. Opt. Phys.* **46** 035202
[46] Jönsson P, Gaigalas G, Bieron J, Fischer C F and Grant I 2013 *Comput. Phys. Commun.* **184** 2197
[47] Fischer C F and Zatsarinny O 2009 *Comput. Phys. Commun.* **180** 879
[48] Visscher L and Dyall K 1997 *At. Data Nucl. Data Tables* **67** 207
[49] Burke V and Noble C 1995 *Comput. Phys. Commun.* **85** 471
[50] Grum-Grzhimailo A 2003 *Comput. Phys. Commun.* **152** 101
[51] Marinković B, Pejčev V, Filipović D, Šević D, Milisavljević S and Predojević B 2007 *Proc. 3rd Int. Conf. on Elementary Processes in Atomic Systems; Radiat. Phys. Chem.* **76** 455
[52] Kim Y-K and Stone P M 2007 *J. Phys. B: At. Mol. Opt. Phys.* **40** 1597
[53] Bray I 1994 *Phys. Rev. Lett.* **73** 1088
[54] Kim Y-K 2001 *Phys. Rev.* A **64** 032713